

Towards Morphologically Induced Anisotropy in Thermally Hysteretic Dielectric Properties of Vanadium Dioxide

Tom G. Mackay*

*School of Mathematics and Maxwell Institute for Mathematical Sciences
University of Edinburgh, Edinburgh EH9 3FD, UK*

and

*NanoMM — Nanoengineered Metamaterials Group
Department of Engineering Science and Mechanics
Pennsylvania State University, University Park, PA 16802-6812, USA*

Akhlesh Lakhtakia

*NanoM — Nanoengineered Metamaterials Group
Department of Engineering Science and Mechanics
Pennsylvania State University, University Park, PA 16802-6812, USA*

Abstract

The Bruggeman homogenization formalism was used to numerically investigate the dielectric properties of a columnar thin film (CTF) made from vanadium dioxide. For visible and near-infrared wavelengths, the CTF is electromagnetically equivalent to a homogeneous orthorhombic material. Over the 58 °C–72 °C temperature range, the eigenvalues of the CTF's relative permittivity dyadic are highly sensitive to temperature, and vary according to whether the CTF is being heated or cooled. The anisotropy revealed through the eigenvalues, and the anisotropy of the associated hysteresis, were investigated in relation to temperature for CTFs of different porosities and columnar cross sections. When the free-space wavelength is 800 nm, the CTF is a dissipative dielectric material that exhibits temperature-dependent anisotropy and anisotropic hysteresis. In contrast, when the free-space wavelength is 1550 nm, the CTF can be either a dissipative dielectric material, a hyperbolic material or a metal-like material, depending on the temperature and the porosity of the CTF. As the porosity of the CTF decreases from 0.55 to 0.3, the anisotropy of the CTF becomes more pronounced, as does the anisotropy of the hysteresis. Only relatively modest variations in anisotropy and hysteresis arise in response to varying the columnar cross-sectional shape, as compared to the variations induced by varying the porosity.

Keywords: Thermal hysteresis; columnar thin film; hyperbolic material; Bruggeman homogenization formalism; anisotropy

1 Introduction

Materials, metamaterials, and metasurfaces with thermally controllable dielectric properties are of interest for numerous applications involving reconfigurable and multifunctional devices [1–4]. Vanadium dioxide

*E-mail: T.Mackay@ed.ac.uk.

(VO₂) is especially interesting in this context as it undergoes a thermally-induced hysteretic phase change over the temperature range 58 °C–72 °C, in the visible, infrared, and terahertz spectral regimes [5–11].

The electromagnetic response of VO₂ is isotropic, as encapsulated by its (complex-valued) relative permittivity $\varepsilon_{\text{VO}_2}$. However, the crystal structure of VO₂ is not cubic — instead, it is monoclinic at temperatures below 58 °C and tetragonal at temperatures above 72 °C [12]. Both monoclinic and tetragonal crystals coexist in varying proportions in the 58 °C–72 °C temperature range. Furthermore, the value of $\varepsilon_{\text{VO}_2}$ for monoclinic VO₂ is significantly different to its value for tetragonal VO₂, at a given free-space wavelength λ_0 .

The transition from monoclinic VO₂ to tetragonal VO₂ can be achieved by heating and it can be reversed by cooling. And this transition is hysteretic. That is, at a temperature in the 58 °C–72 °C range, the value of $\varepsilon_{\text{VO}_2}$ depends on whether VO₂ was heated up or cooled down to reach that temperature [13]. Since VO₂ is hysteretically biphasic, $\varepsilon_{\text{VO}_2}$ may be regarded as a double-valued function of temperature; hence, we write $\varepsilon_{\text{VO}_2} = \varepsilon_{\text{VO}_2}^{\text{heat}}$ for the heating phase and $\varepsilon_{\text{VO}_2} = \varepsilon_{\text{VO}_2}^{\text{cool}}$ for the cooling phase.

The prospect of an anisotropic material, metamaterial or metasurface whose dielectric properties for propagation in different directions are thermally controllable presents opportunities for directional control and tuning in applications involving reconfigurable and multifunctional devices. How could such a prospect be realized? A practical means of realizing thermal directional control is to use VO₂ to fabricate a columnar thin film (CTF) [14–16]. A CTF is a forest of parallel columns, inclined at a certain angle to a substrate upon which they are deposited by a technique such as oblique angle deposition. Macroscopically, a CTF is electromagnetically equivalent to a homogeneous anisotropic material with orthorhombic symmetry.

In the following sections, the Bruggeman homogenization formalism [17–19] is employed to estimate the relative permittivity parameters of a CTF made from VO₂, and the effects of temperature on anisotropy and on the anisotropy of hysteresis are thereby investigated. The following notation is adopted: 3-vectors are underlined once and 3×3 dyadics are underlined twice. The triad of Cartesian basis vectors is denoted as $\{\underline{\hat{u}}_x, \underline{\hat{u}}_y, \underline{\hat{u}}_z\}$.

2 Homogenization model of columnar thin film

2.1 Preliminaries

A bulk material is evaporated and a collimated vapor flux is directed in a low-pressure chamber towards a planar substrate to form a CTF [14, 15, 20, 21]. Suppose that the planar substrate is parallel to the xy plane, and the bulk material is VO₂ with relative permittivity $\varepsilon_{\text{VO}_2}$. Provided that wavelengths are much greater than the cross-sectional dimensions of the CTF columns, the CTF may be regarded as a homogeneous orthorhombic material which is characterized by the frequency-domain constitutive relation [14, 15, 21]

$$\underline{D} = \varepsilon_0 \underline{\underline{\varepsilon}}_{\text{CTF}} \cdot \underline{E}. \quad (1)$$

Herein, the CTF's relative permittivity dyadic is

$$\underline{\underline{\varepsilon}}_{\text{CTF}} = \underline{\underline{S}}_y(\chi) \cdot (\varepsilon_a \underline{\hat{u}}_z \underline{\hat{u}}_z + \varepsilon_b \underline{\hat{u}}_x \underline{\hat{u}}_x + \varepsilon_c \underline{\hat{u}}_y \underline{\hat{u}}_y) \cdot \underline{\underline{S}}_y^{-1}(\chi), \quad (2)$$

which has eigenvalues $\{\varepsilon_a, \varepsilon_b, \varepsilon_c\}$, and ε_0 is the permittivity of free space. The parallel columns of the CTF are inclined to the xy plane at an angle $\chi \in (0, \pi/2]$, as prescribed by the inclination dyadic

$$\underline{\underline{S}}_y(\chi) = \underline{\hat{u}}_y \underline{\hat{u}}_y + (\underline{\hat{u}}_x \underline{\hat{u}}_x + \underline{\hat{u}}_z \underline{\hat{u}}_z) \cos \chi + (\underline{\hat{u}}_z \underline{\hat{u}}_x - \underline{\hat{u}}_x \underline{\hat{u}}_z) \sin \chi. \quad (3)$$

Note that $\varepsilon_{a,b,c}$ and χ depend on the direction of the collimated vapor flux with respect to the xy plane [14], and that $\varepsilon_{a,b,c}$ also depend on λ_0 .

From the perspective of homogenization theory, each column of the CTF can be viewed as a string of elongated ellipsoidal inclusions [15, 22]. All inclusions have the same orientation, and the same shape as prescribed by the shape dyadic

$$\underline{\underline{u}}_n \underline{\underline{u}}_n + \gamma_\tau \underline{\underline{u}}_\tau \underline{\underline{u}}_\tau + \gamma_b \underline{\underline{u}}_b \underline{\underline{u}}_b, \quad (4)$$

wherein

$$\left. \begin{aligned} \underline{u}_n &= -\hat{u}_x \sin \chi + \hat{u}_z \cos \chi \\ \underline{u}_\tau &= \hat{u}_x \cos \chi + \hat{u}_z \sin \chi \\ \underline{u}_b &= -\hat{u}_y \end{aligned} \right\} \quad (5)$$

are the normal, tangential, and binormal basis vectors, respectively. The columns of the CTF are needlelike. Accordingly, the shape parameters $\gamma_b \gtrsim 1$ and $\gamma_\tau \gg 1$. For slim inclusions, increasing γ_τ beyond 10 has negligible effect; hence, $\gamma_\tau = 15$ is assumed. A schematic representation of such a CTF is presented in Fig. 1.

The void region between columns of the CTF is filled with air, which is taken to be electromagnetically equivalent to free space (or vacuum). The fraction of the CTF's volume that is occupied by ellipsoidal inclusions is denoted f . Since $f \in (0, 1)$, the porosity of the CTF is given as $1 - f$.

2.2 Bruggeman homogenization formalism

The eigenvalues $\{\varepsilon_a, \varepsilon_b, \varepsilon_c\}$ of $\underline{\underline{\varepsilon}}_{CTF}$ that characterize the CTF at macroscopic length scales can be estimated from the parameters ε_{VO_2} , f , and γ_b that characterize the CTF at microscopic length scales by means of the Bruggeman homogenization formalism. The Bruggeman formalism has the advantage over other commonly used homogenization formalisms, e.g., the Maxwell Garnett formalism [18], insofar as it treats the deposited material region and the void region symmetrically. Consequently, there are no restrictions on the value of $f \in (0, 1)$.

The polarizability density dyadic relevant to the deposited material (i.e., ε_{VO_2}) is [19]

$$\begin{aligned} \underline{\underline{a}}_d &= [\varepsilon_{VO_2} \underline{\underline{I}} - (\varepsilon_a \hat{u}_z \hat{u}_z + \varepsilon_b \hat{u}_x \hat{u}_x + \varepsilon_c \hat{u}_y \hat{u}_y)] \\ &\quad \cdot \left\{ \underline{\underline{I}} + \underline{\underline{D}}_d \cdot [\varepsilon_{VO_2} \underline{\underline{I}} - (\varepsilon_a \hat{u}_z \hat{u}_z + \varepsilon_b \hat{u}_x \hat{u}_x + \varepsilon_c \hat{u}_y \hat{u}_y)] \right\}^{-1}, \end{aligned} \quad (6)$$

while the polarizability density dyadic relevant to the void medium (i.e., air) is

$$\begin{aligned} \underline{\underline{a}}_v &= [\underline{\underline{I}} - (\varepsilon_a \hat{u}_z \hat{u}_z + \varepsilon_b \hat{u}_x \hat{u}_x + \varepsilon_c \hat{u}_y \hat{u}_y)] \\ &\quad \cdot \left\{ \underline{\underline{I}} + \underline{\underline{D}}_v \cdot [\underline{\underline{I}} - (\varepsilon_a \hat{u}_z \hat{u}_z + \varepsilon_b \hat{u}_x \hat{u}_x + \varepsilon_c \hat{u}_y \hat{u}_y)] \right\}^{-1}, \end{aligned} \quad (7)$$

wherein the corresponding depolarization dyadics

$$\underline{\underline{D}}_d = \frac{2}{\pi} \int_{\phi=0}^{\pi/2} d\phi \int_{\theta=0}^{\pi/2} d\theta \sin \theta \frac{\frac{\cos^2 \theta}{\gamma_\tau^2} \hat{u}_x \hat{u}_x + \sin^2 \theta \left(\cos^2 \phi \hat{u}_z \hat{u}_z + \frac{\sin^2 \phi}{\gamma_b^2} \hat{u}_y \hat{u}_y \right)}{\varepsilon_b \frac{\cos^2 \theta}{\gamma_\tau^2} + \sin^2 \theta \left(\varepsilon_a \cos^2 \phi + \varepsilon_c \frac{\sin^2 \phi}{\gamma_b^2} \right)} \quad (8)$$

and

$$\underline{\underline{D}}_v = \frac{2}{\pi} \int_{\phi=0}^{\pi/2} d\phi \int_{\theta=0}^{\pi/2} d\theta \sin \theta \frac{\cos^2 \theta \hat{u}_x \hat{u}_x + \sin^2 \theta \left(\cos^2 \phi \hat{u}_z \hat{u}_z + \sin^2 \phi \hat{u}_y \hat{u}_y \right)}{\varepsilon_b \cos^2 \theta + \sin^2 \theta \left(\varepsilon_a \cos^2 \phi + \varepsilon_c \sin^2 \phi \right)}. \quad (9)$$

The essence of the Bruggeman formalism is that the volume-fraction-weighted sum of the two polarizability density dyadics is null valued [19]; i.e.,

$$f \underline{\underline{a}}_d + (1 - f) \underline{\underline{a}}_v = \underline{\underline{0}}, \quad (10)$$

with $\underline{\underline{0}}$ being the 3×3 null dyadic. The eigenvalues $\{\varepsilon_a, \varepsilon_b, \varepsilon_c\}$ of $\underline{\underline{\varepsilon}}_{CTF}$ can be extracted from the Bruggeman eqn. (10) by numerical means, such as the Jacobi method [23], provided that ε_{VO_2} , f , and γ_b are known [22].

3 Numerical studies

The refractive index of VO_2 was determined by Cormier *et al.* [13] for heating and cooling phases over the temperature range 55°C – 75°C , for $\lambda_0 \in \{800, 1550\}$ nm. Plots of the corresponding real and imaginary

parts of $\varepsilon_{\text{VO}_2}$ versus temperature are provided in Fig. 2, with $\varepsilon_{\text{VO}_2}^{\text{heat}}$ and $\varepsilon_{\text{VO}_2}^{\text{cool}}$ denoting the values of $\varepsilon_{\text{VO}_2}$ for the heating and cooling phases, respectively. Let $\varepsilon_{\text{VO}_2}^{55^\circ\text{C}}$ and $\varepsilon_{\text{VO}_2}^{75^\circ\text{C}}$ denote the values of $\varepsilon_{\text{VO}_2}$ at 55°C and 75°C , respectively. Plots of the measures of hysteresis

$$\left. \begin{aligned} \Delta_{\text{VO}_2}^{\text{Re}} &= \text{Re} \{ \varepsilon_{\text{VO}_2}^{\text{heat}} \} - \text{Re} \{ \varepsilon_{\text{VO}_2}^{\text{cool}} \} \\ \Delta_{\text{VO}_2}^{\text{Im}} &= \text{Im} \{ \varepsilon_{\text{VO}_2}^{\text{heat}} \} - \text{Im} \{ \varepsilon_{\text{VO}_2}^{\text{cool}} \} \end{aligned} \right\} \quad (11)$$

and relative measures of hysteresis

$$\left. \begin{aligned} \hat{\Delta}_{\text{VO}_2}^{\text{Re}} &= \frac{\Delta_{\text{VO}_2}^{\text{Re}}}{|\text{Re} \{ \varepsilon_{\text{VO}_2}^{75^\circ\text{C}} \} - \text{Re} \{ \varepsilon_{\text{VO}_2}^{55^\circ\text{C}} \}|} \\ \hat{\Delta}_{\text{VO}_2}^{\text{Im}} &= \frac{\Delta_{\text{VO}_2}^{\text{Im}}}{|\text{Im} \{ \varepsilon_{\text{VO}_2}^{75^\circ\text{C}} \} - \text{Im} \{ \varepsilon_{\text{VO}_2}^{55^\circ\text{C}} \}|} \end{aligned} \right\} \quad (12)$$

versus temperature are also provided in Fig. 2.

For $\lambda_0 = 800$ nm, $\text{Re} \{ \varepsilon_{\text{VO}_2} \}$ and $\text{Im} \{ \varepsilon_{\text{VO}_2} \}$ exhibit hysteresis over the approximate temperature range 60°C – 71°C . In the thermal-hysteresis regime, $\text{Re} \{ \varepsilon_{\text{VO}_2}^{\text{heat}} \} > \text{Re} \{ \varepsilon_{\text{VO}_2}^{\text{cool}} \}$ whereas $\text{Im} \{ \varepsilon_{\text{VO}_2}^{\text{heat}} \} < \text{Im} \{ \varepsilon_{\text{VO}_2}^{\text{cool}} \}$. Also, the maximum magnitude of $\Delta_{\text{VO}_2}^{\text{Re}}$ is substantially larger than the maximum magnitude of $\Delta_{\text{VO}_2}^{\text{Im}}$ but the maximum magnitude of $\hat{\Delta}_{\text{VO}_2}^{\text{Re}}$ is substantially smaller than the maximum magnitude of $\hat{\Delta}_{\text{VO}_2}^{\text{Im}}$. That is, the hysteresis is more pronounced for the real part of $\varepsilon_{\text{VO}_2}$ than for the imaginary part of $\varepsilon_{\text{VO}_2}$, but the relative hysteresis is more pronounced for the imaginary part of $\varepsilon_{\text{VO}_2}$ than for the real part of $\varepsilon_{\text{VO}_2}$.

The nature of the thermal hysteresis for $\lambda_0 = 1550$ nm is qualitatively similar to that for $\lambda_0 = 800$ nm, but

- the thermal-hysteresis regime is slightly wider;
- the maximum magnitudes of $\Delta_{\text{VO}_2}^{\text{Re}}$ and $\Delta_{\text{VO}_2}^{\text{Im}}$ are substantially larger;
- the maximum magnitude of $\hat{\Delta}_{\text{VO}_2}^{\text{Re}}$ is slightly larger and the maximum magnitude of $\hat{\Delta}_{\text{VO}_2}^{\text{Im}}$ is substantially smaller

for $\lambda_0 = 1550$ nm than for $\lambda_0 = 800$ nm. Also, for $\lambda_0 = 1550$ nm, the maximum magnitude of $\Delta_{\text{VO}_2}^{\text{Re}}$ is approximately the same as that of $\Delta_{\text{VO}_2}^{\text{Im}}$ and likewise the maximum magnitude of $\hat{\Delta}_{\text{VO}_2}^{\text{Re}}$ is approximately the same as that of $\hat{\Delta}_{\text{VO}_2}^{\text{Im}}$; i.e., the hysteresis and relative hysteresis are approximately equally pronounced for the real and imaginary parts of $\varepsilon_{\text{VO}_2}$. Another notable difference is that $\text{Re} \{ \varepsilon_{\text{VO}_2}^{\text{heat}} \} > 0$ and $\text{Re} \{ \varepsilon_{\text{VO}_2}^{\text{cool}} \} > 0$ across the entire temperature range considered for $\lambda_0 = 800$ nm but, for $\lambda_0 = 1550$ nm, $\text{Re} \{ \varepsilon_{\text{VO}_2}^{\text{heat}} \} > 0$ in the temperature range 55°C – 69.5°C and $\text{Re} \{ \varepsilon_{\text{VO}_2}^{\text{heat}} \} < 0$ at higher temperatures, and $\text{Re} \{ \varepsilon_{\text{VO}_2}^{\text{cool}} \} > 0$ in the temperature range 55°C – 63.5°C and $\text{Re} \{ \varepsilon_{\text{VO}_2}^{\text{cool}} \} < 0$ at higher temperatures. That is, VO_2 is a dissipative dielectric material across the entire temperature range considered for $\lambda_0 = 800$ nm, but it is a dissipative dielectric material at low temperatures and becomes metal-like at higher temperatures for $\lambda_0 = 1550$ nm. Furthermore, the temperature at which the transition between as dissipative dielectric material and a metal-like material occurs depends upon whether the material is being heated or cooled.

Next we turn to the VO_2 CTFs. We begin by setting $\gamma_b = 1.5$ and $f = 0.6$, which are typical values for CTFs made from a range of different materials [22]; the effects of varying γ_b and f are explored later in this section. For $\lambda_0 = 800$ nm, plots of the Bruggeman estimates of the real and imaginary parts of ε_a , ε_b , and ε_c (for both heating and cooling phases) versus temperature are presented in Fig. 3. Therein, $\varepsilon_{a,b,c}^{\text{heat}}$ and $\varepsilon_{a,b,c}^{\text{cool}}$ denote the values of $\varepsilon_{a,b,c}$ for the heating and cooling phases, respectively.

The orthorhombic symmetry of the CTF is apparent since, for both heating and cooling phases, the values of ε_b are clearly different from the values of ε_a and ε_c , and there are smaller differences between the

values of ε_a and ε_c . In addition, both the real and imaginary parts of ε_a , ε_b , and ε_c exhibit thermal hysteresis to varying degrees. Plots of the measures of hysteresis

$$\left. \begin{aligned} \Delta_\ell^{\text{Re}} &= \text{Re} \{ \varepsilon_\ell^{\text{heat}} \} - \text{Re} \{ \varepsilon_\ell^{\text{cool}} \} \\ \Delta_\ell^{\text{Im}} &= \text{Im} \{ \varepsilon_\ell^{\text{heat}} \} - \text{Im} \{ \varepsilon_\ell^{\text{cool}} \} \end{aligned} \right\}, \quad \ell \in \{a, b, c\} \quad (13)$$

and relative measures of hysteresis

$$\left. \begin{aligned} \hat{\Delta}_\ell^{\text{Re}} &= \frac{\Delta_\ell^{\text{Re}}}{|\text{Re} \{ \varepsilon_\ell^{75^\circ\text{C}} \} - \text{Re} \{ \varepsilon_\ell^{55^\circ\text{C}} \}|} \\ \hat{\Delta}_\ell^{\text{Im}} &= \frac{\Delta_\ell^{\text{Im}}}{|\text{Im} \{ \varepsilon_\ell^{75^\circ\text{C}} \} - \text{Im} \{ \varepsilon_\ell^{55^\circ\text{C}} \}|} \end{aligned} \right\}, \quad \ell \in \{a, b, c\} \quad (14)$$

versus temperature are also presented in Fig. 3. Herein, $\varepsilon_\ell^{55^\circ\text{C}}$ and $\varepsilon_\ell^{75^\circ\text{C}}$ denote the values of ε_ℓ at 55°C and 75°C , respectively, with $\ell \in \{a, b, c\}$. The maximum magnitude of Δ_b^{Re} is substantially larger than the maximum magnitude of Δ_c^{Re} which, in turn, is substantially larger than the maximum magnitude of Δ_a^{Re} . Also, the maximum magnitude of Δ_b^{Im} is slightly larger than the maximum magnitude of Δ_c^{Im} which, in turn, is slightly larger than the maximum magnitude of Δ_a^{Im} . As regards the relative measures of hysteresis, the maximum of $|\hat{\Delta}_b^{\text{Im}}|$ is substantially larger than the maximum of $|\hat{\Delta}_c^{\text{Im}}|$ which, in turn, is substantially larger than the maximum of $|\hat{\Delta}_a^{\text{Im}}|$; in contrast, the plots for $\hat{\Delta}_a^{\text{Re}}$, $\hat{\Delta}_b^{\text{Re}}$, and $\hat{\Delta}_c^{\text{Re}}$ are all similar. Thus, thermal hysteresis has been transformed from isotropic for bulk VO_2 to anisotropic for the VO_2 CTF.

The computations for Fig. 3 were repeated for $\lambda_0 = 1550$ nm and the results plotted in Fig. 4. As regards anisotropy and hysteresis, the results for $\lambda_0 = 1550$ nm displayed in Fig. 4 are qualitatively similar to those for $\lambda_0 = 800$ nm displayed in Fig. 3, but

- the anisotropy of the CTF is substantially more pronounced and
- the anisotropy of the thermal hysteresis, but not of the relative thermal hysteresis, is substantially more pronounced

for $\lambda_0 = 1550$ nm.

However, there is an important difference in the nature of the VO_2 CTF for $\lambda_0 = 1550$ nm as compared to its nature for $\lambda_0 = 800$ nm. According to Fig. 3, the real parts of ε_a , ε_b , and ε_c (for both heating and cooling phases) are all positive valued for $\lambda_0 = 800$ nm across the entire temperature range considered. According to Fig. 4, the same is true for ε_a and ε_c for $\lambda_0 = 1550$ nm, but $\text{Re} \{ \varepsilon_b^{\text{heat}} \}$ is positive valued only for the temperature range 55°C – 71°C and negative valued at higher temperatures, and $\text{Re} \{ \varepsilon_b^{\text{cool}} \}$ is positive valued only for the temperature range 55°C – 65°C and negative valued at higher temperatures. That is, the CTF is a dissipative dielectric material for $\lambda_0 = 800$ nm across the entire temperature range considered, it is a dissipative dielectric material only at low temperatures and becomes a hyperbolic material [24] at higher temperatures for $\lambda_0 = 1550$ nm. Furthermore, the temperature at which the dissipative dielectric material/hyperbolic material transition occurs depends upon whether the material is being heated or cooled.

Now let us explore the effect of varying f . In order to appreciate more easily the effects of the variation on the anisotropy of the CTF, λ_0 was fixed at 1550 nm. Since there can be no anisotropy for $f \in \{0, 1\}$, we confined our attention to mid-range values of f . The computations for Fig. 4 were repeated for $f \in \{0.45, 0.66, 0.7\}$ and the results plotted in Fig. 5. As regards anisotropy and hysteresis, the results for $f \in \{0.45, 0.66, 0.7\}$ displayed in Fig. 5 are qualitatively similar to those for $f = 0.6$ displayed in Fig. 4, but certain trends are apparent: the anisotropy of the CTF becomes substantially more pronounced as the value of f increases and the anisotropy of the hysteresis, but not of the relative hysteresis, becomes substantially more pronounced as the value of f increases. In addition, there are important differences in the natures of the CTFs for each of $f = 0.45, 0.6, 0.66$, and 0.7 :

- (i) for $f = 0.45$, $\text{Re} \{ \varepsilon_a \} > 0$, $\text{Re} \{ \varepsilon_b \} > 0$, and $\text{Re} \{ \varepsilon_c \} > 0$ across the entire temperature range considered;

- (ii) for $f = 0.6$, as discussed earlier in connection with Fig. 4, $\text{Re}\{\varepsilon_a\} > 0$ and $\text{Re}\{\varepsilon_c\} > 0$ across the entire temperature range considered but $\text{Re}\{\varepsilon_b^{\text{heat}}\} > 0$ only for the temperature range 55°C – 71°C and $\text{Re}\{\varepsilon_b^{\text{cool}}\} > 0$ only for the temperature range 55°C – 65°C ;
- (iii) for $f = 0.66$, $\text{Re}\{\varepsilon_a\} > 0$ across the entire temperature range considered but $\text{Re}\{\varepsilon_b^{\text{heat}}\} > 0$ only for the temperature range 55°C – 70.5°C and $\text{Re}\{\varepsilon_b^{\text{cool}}\} > 0$ only for the temperature range 55°C – 64°C ; and $\text{Re}\{\varepsilon_c^{\text{heat}}\} > 0$ only for the temperature range 55°C – 72°C and $\text{Re}\{\varepsilon_c^{\text{cool}}\} > 0$ only for the temperature range 55°C – 66°C ;
- (iv) for $f = 0.7$, $\text{Re}\{\varepsilon_a^{\text{heat}}\} > 0$ only for the temperature range 55°C – 71°C and $\text{Re}\{\varepsilon_a^{\text{cool}}\} > 0$ only for the temperature range 55°C – 65.5°C ; $\text{Re}\{\varepsilon_b^{\text{heat}}\} > 0$ only for the temperature range 55°C – 70°C and $\text{Re}\{\varepsilon_b^{\text{cool}}\} > 0$ only for the temperature range 55°C – 64°C ; and $\text{Re}\{\varepsilon_c^{\text{heat}}\} > 0$ only for the temperature range 55°C – 70.5°C and $\text{Re}\{\varepsilon_c^{\text{cool}}\} > 0$ only for the temperature range 55°C – 64.5°C .

In other words, the CTF is always a dissipative dielectric material at temperatures close to 55°C , for all values of f considered; but at temperatures close to 75°C the CTF can be (a) a dissipative dielectric material, (b) a hyperbolic material, or (c) a metal-like material, depending on the value of f . Furthermore, the temperature at which the dissipative dielectric material/hyperbolic material transition or the hyperbolic material/metal-like material transition occurs depends upon whether the material is being heated or cooled.

Lastly let us explore the effect of varying γ_b . As for Fig. 5, λ_0 was fixed at 1550 nm in order to appreciate more easily the effects of the variation on the anisotropy of the CTF. The computations for Fig. 4 were repeated for $\gamma_b \in \{1, 5\}$ and the results plotted in Fig. 6. The columns of the CTF are circular in cross section when $\gamma_b = 1$ but like blades when $\gamma_b = 5$ [25]. As regards anisotropy and hysteresis, the results for $\gamma_b \in \{1, 5\}$ displayed in Fig. 6 are qualitatively similar to those for $\gamma_b = 1.5$ displayed in Fig. 4, but there are certain notable features: When $\gamma_b = 1$, $\varepsilon_a = \varepsilon_c$ for both heating and cooling phases; correspondingly, the CTF is a uniaxial material with distinguished axis parallel to \underline{u}_τ . When $\gamma_b = 5$, $\varepsilon_b \approx \varepsilon_c$ for both heating and cooling phases; correspondingly, the CTF is very close to being a uniaxial material with distinguished axis parallel to \underline{u}_n . Only relatively modest variations in anisotropy and hysteresis arise as γ_b increases from 1 to 5, as compared to the variations induced by varying f .

4 Closing remarks

The Bruggeman homogenization formalism was used to numerically investigate the anisotropic dielectric properties of a CTF made from VO_2 . In the visible and near-infrared spectral regimes, the CTF is electromagnetically equivalent to a homogeneous orthorhombic material, characterized by the relative permittivity dyadic $\underline{\underline{\varepsilon}}_{\text{CTF}}$ with eigenvalues $\{\varepsilon_a, \varepsilon_b, \varepsilon_c\}$. Over the temperature range 58°C – 72°C , $\{\varepsilon_a, \varepsilon_b, \varepsilon_c\}$ are highly sensitive to temperature, and vary according to whether the CTF is being heated or cooled. The anisotropy revealed through $\{\varepsilon_a, \varepsilon_b, \varepsilon_c\}$, and the anisotropy of the associated hysteresis, were investigated as a function of temperature for CTFs of different porosities and of different column shapes. The CTF is a dissipative dielectric material that exhibits temperature-dependent anisotropy and anisotropic hysteresis, for $\lambda_0 = 800\text{ nm}$. In contrast, for $\lambda_0 = 1550\text{ nm}$, the CTF can be either a dissipative dielectric material, a hyperbolic material or a metal-like material, depending on the temperature and on the porosity of the CTF.

The ability to modulate the anisotropy of a CTF made from VO_2 with temperature is an attractive feature when considering directional control and tuning for applications involving reconfigurable and multifunctional devices. Furthermore, the ability to modulate anisotropic thermal hysteresis may be an attractive feature for directional control in optical/infrared switching applications. And the prospect of thermally controlling whether a CTF is a dissipative dielectric material, a hyperbolic material or a metal-like material should present additional opportunities [26, 27].

Acknowledgments: TGM was supported by EPSRC (grant number EP/V046322/1). AL was supported by the US National Science Foundation (grant number DMS-1619901) as well as the Charles Godfrey Binder

References

- [1] Q. Wang, E. T. Rogers, B. Gholipour, C.-M. Wang, G. Yuan, J. Teng, and N. I. Zheludev, “Optically reconfigurable metasurfaces and photonic devices based on phase change materials,” *Nat. Photon.* **10**, 60–65 (2016).
- [2] E. Maguid, I. Yulevich, M. Yannai, V. Kleiner, M. L. Brongersma, and E. Hasman, “Multifunctional interleaved geometric-phase dielectric metasurfaces,” *Light Sci. Appl.* **6**, e17027 (2017).
- [3] A. Lakhtakia, D. E. Wolfe, M. W. Horn, J. Mazurowski, A. Burger, and P. Banerjee, “Bioinspired multicontrollable metasurfaces and metamaterials for terahertz applications,” *Proc. SPIE* **10162**, 101620V (2017).
- [4] W. Huang, X. Yin, C. Huang, Q. Wang, T. Miao, and Y. Zhu, “Optical switching of a metamaterial by temperature controlling,” *Appl. Phys. Lett.* **96**, 261908 (2010).
- [5] M. J. Dicken, K. Aydin, I. M. Pryce, L. A. Sweatlock, E. M. Boyd, S. Walavalkar, J. Ma, and H. A. Atwater, “Frequency tunable near-infrared metamaterials based on VO₂ phase transition,” *Opt. Exp.* **17**, 18330–18339 (2009).
- [6] G. Seo, B. Kim, Y. W. Lee, and H. Kim, “Photo-assisted bistable switching using Mott transition in two-terminal VO₂ device,” *Appl. Phys. Lett.* **100**, 011908 (2012).
- [7] S. Bonora, G. Beydaghyan, A. Haché, and P.V. Ashrit, “Mid-IR laser beam quality measurement through vanadium dioxide optical switching,” *Opt. Lett.* **38**, 1554–1556 (2013).
- [8] S. Cueff, J. John, Z. Zhang, J. Parra, J. Sun, R. Orobtcchouk, S. Ramanathan, and P. Sanchis, “VO₂ nanophotonics,” *APL Photon.* **5**, 110901 (2020).
- [9] A. E. Serebryannikov, A. Lakhtakia, G. A. E. Vandenbosch, and E. Ozbay, “Transmissive terahertz metasurfaces with vanadium dioxide split-rings and grids for switchable asymmetric polarization manipulation,” *Sci. Rep.* **12**, 3518 (2022).
- [10] H. Lu, S. Clark, Y. Guo, and J. Robertson, “The metal-insulator phase change in vanadium dioxide and its applications,” *J. Appl. Phys.* **129**, 240902 (2021).
- [11] R. Shi, N. Shen, J. Wang, W. Wang, A. Amini, N. Wang, and C. Cheng, “Recent advances in fabrication strategies, phase transition modulation, and advanced applications of vanadium dioxide,” *Appl. Phys. Rev.* **6**, 011312 (2019).
- [12] F.J. Morin, “Oxides which show a metal-to-insulator transition at the Néel temperature,” *Phys. Rev. Lett.* **3**, 34–36 (1959).
- [13] P. Cormier, T.V. Son, J. Thibodeau, A. Doucet, V.-V. Truong, and A. Haché, “Vanadium dioxide as a material to control light polarization in the visible and near infrared,” *Opt. Commun.* **382**, 80–85 (2017).
- [14] I. J. Hodgkinson and Q. h. Wu, *Birefringent Thin Films and Polarizing Elements* (World Scientific, Singapore, 1997).
- [15] A. Lakhtakia and R. Messier, *Sculptured Thin Films: Nanoengineered Morphology and Optics* (SPIE Press, Bellingham, WA, USA, 2005).

- [16] S. Bhupathi, M. Abutoama, Y. Long and I. Abdulhalim, “Sculptured thin film vanadium dioxide thermochromic coatings grown by oblique angle deposition: investigation of transmittance response and modulation enhancement by experiment and theoretical modeling,” *J. Mater. Chem. C* **9**, 13304 (2021).
- [17] S.K. Kanaun, Self-consistent schemes in the problem of electromagnetic wave propagation through dielectric media with isolated inhomogeneities, *Wave Motion* **27** (1998) 355–378.
- [18] L. Ward, *The Optical Constants of Bulk Materials and Films, 2nd Edition* (IOP Publishing, Bristol, UK, 2000).
- [19] T. G. Mackay and A. Lakhtakia, *Modern Analytical Electromagnetic Homogenization with Mathematica*, 2nd Edition (IOP Publishing, Bristol, UK, 2020).
- [20] B. D. Gauntt, E. C. Dickey, and M. W. Horn, “Stoichiometry and microstructural effects on electrical conduction in pulsed dc sputtered vanadium oxide thin films,” *J. Mater. Res.* **24**, 1590–1599 (2009).
- [21] V. Vepachedu, P. D. McAtee, and A. Lakhtakia, “Nonexhibition of Bragg phenomenon by chevronic sculptured thin films: experiment and theory,” *J. Nanophoton.* **11**, 036018 (2017).
- [22] T. G. Mackay and A. Lakhtakia, “Determination of constitutive and morphological parameters of columnar thin films by inverse homogenization,” *J. Nanophoton.* **4**, 041535 (2010).
- [23] B. Michel, “Recent developments in the homogenization of linear bianisotropic composite materials,” in: Eds. O. N. Singh and A. Lakhtakia, *Electromagnetic Fields in Unconventional Materials and Structures* (Wiley, New York, NY, USA, 2000, pp. 39–82).
- [24] I. Smolyaninov, *Hyperbolic Metamaterials* (Morgan & Claypool, San Rafael, CA, USA, 2018).
- [25] F. Tang, T. Parker, H.-F. Li, G.-C. Wang, and T.-M. Lu, “Unusual magnesium crystalline nanoblades grown by oblique angle vapor deposition,” *J. Nanosci. Nanotechnol.* **7**, 3239–3244 (2007).
- [26] O. Takayama, and A. V. Lavrinenko, “Optics with hyperbolic materials,” *J. Opt. Soc. Am. B* **36**, F38–F48 (2019).
- [27] M. V. Davidovich, “Hyperbolic metamaterials: production, properties, applications, and prospects,” *Phys. Usp.* **62**, 1173–1207 (2019).

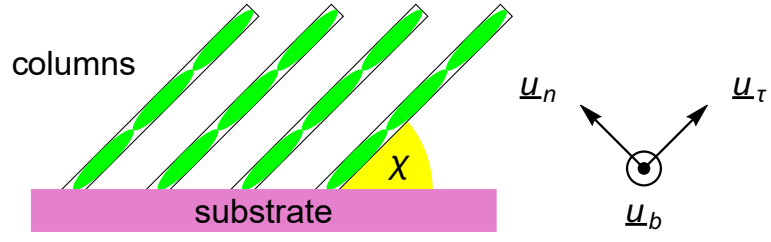


Figure 1: Schematic representation of a CTF with columns inclined at angle χ to the planar substrate.

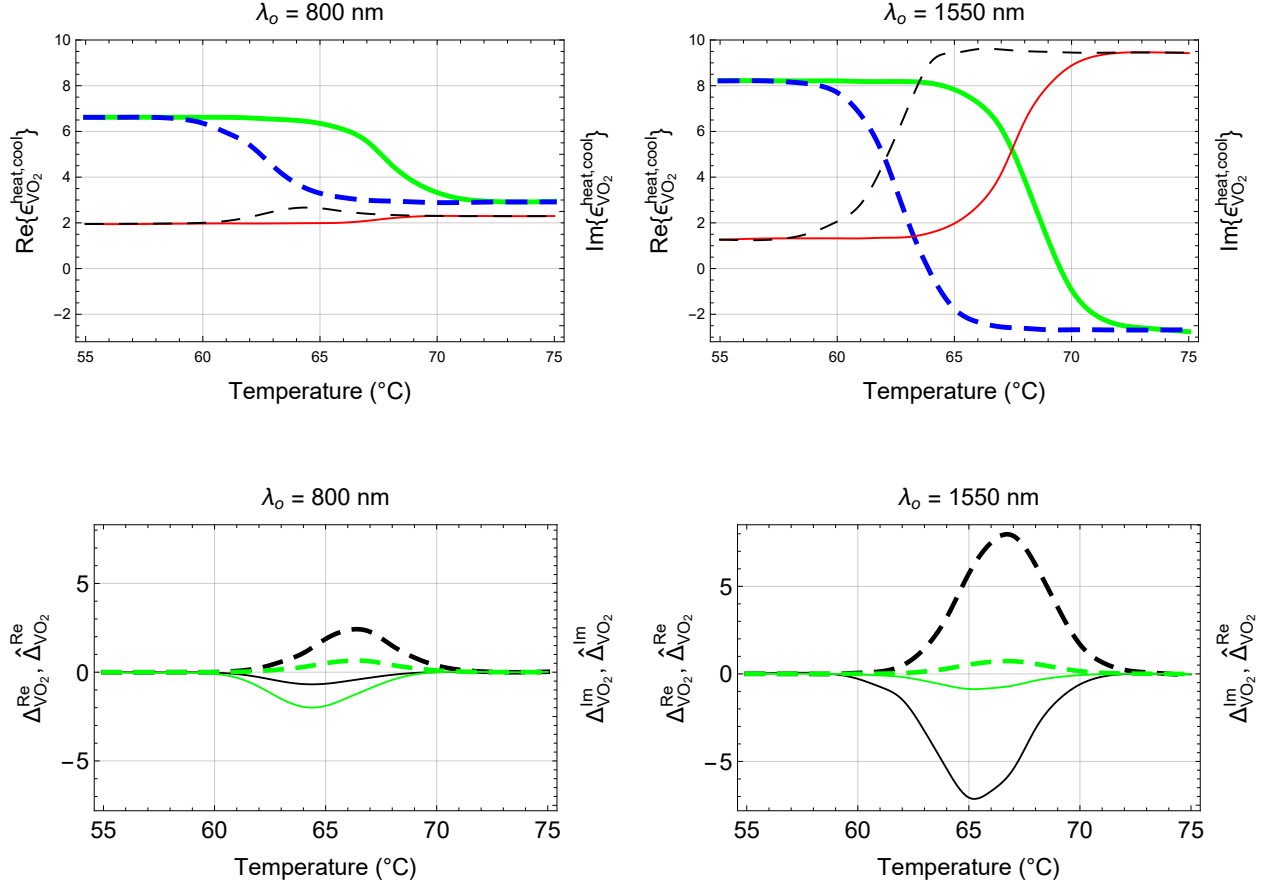


Figure 2: Real and imaginary parts of $\epsilon_{VO_2}^{\text{heat,cool}}$ plotted against temperature (derived from Fig. 4 of Ref. 13), for $\lambda_0 \in \{800, 1550\}$ nm. Also plotted against temperature are $\Delta_{VO_2}^{\text{Re}}$, $\hat{\Delta}_{VO_2}^{\text{Re}}$, $\Delta_{VO_2}^{\text{Im}}$, and $\hat{\Delta}_{VO_2}^{\text{Im}}$. Key: $\text{Re}\{\epsilon_{VO_2}^{\text{heat}}\}$: thick green solid curve; $\text{Re}\{\epsilon_{VO_2}^{\text{cool}}\}$: thick blue dashed curve; $\text{Im}\{\epsilon_{VO_2}^{\text{heat}}\}$: thin red solid curve; $\text{Im}\{\epsilon_{VO_2}^{\text{cool}}\}$: thin black dashed curve; $\Delta_{VO_2}^{\text{Re}}$: thick black dashed curve; $\hat{\Delta}_{VO_2}^{\text{Re}}$: thick green dashed curve; $\Delta_{VO_2}^{\text{Im}}$: thin black solid curve; $\hat{\Delta}_{VO_2}^{\text{Im}}$: thin green solid curve;

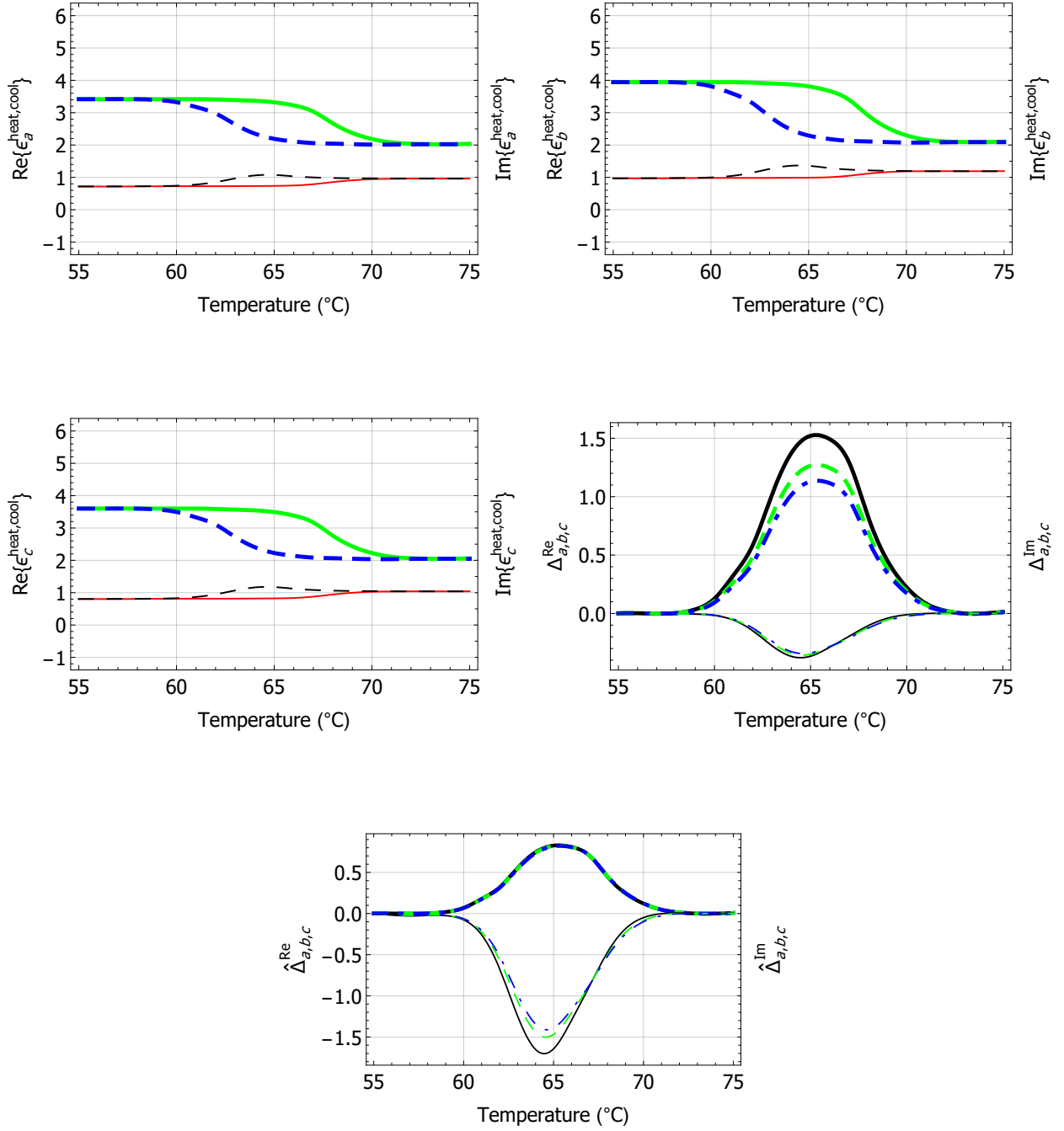


Figure 3: Real and imaginary parts of the CTF's relative permittivity scalars $\epsilon_{a,b,c}^{\text{heat,cool}}$ estimated using the Bruggeman homogenization formalism plotted against temperature for $\lambda_0 = 800$ nm, with $\gamma_\tau = 15$, $\gamma_b = 1.5$, and $f = 0.6$. Also plotted against temperature are $\Delta_{a,b,c}^{\text{Re}}$, $\Delta_{a,b,c}^{\text{Im}}$, $\hat{\Delta}_{a,b,c}^{\text{Re}}$ and $\hat{\Delta}_{a,b,c}^{\text{Im}}$. Key: $\text{Re}\{\epsilon_{a,b,c}^{\text{heat}}\}$: thick green solid curve; $\text{Re}\{\epsilon_{a,b,c}^{\text{cool}}\}$: thick blue dashed curve; $\text{Im}\{\epsilon_{a,b,c}^{\text{heat}}\}$: thin red solid curve; $\text{Im}\{\epsilon_{a,b,c}^{\text{cool}}\}$: thin black dashed curve; Δ_a^{Re} , $\hat{\Delta}_a^{\text{Re}}$: thick blue broken dashed curve; Δ_b^{Re} , $\hat{\Delta}_b^{\text{Re}}$: thick black solid curve; Δ_c^{Re} , $\hat{\Delta}_c^{\text{Re}}$: thick green dashed curve; Δ_a^{Im} , $\hat{\Delta}_a^{\text{Im}}$: thin blue broken dashed curve; Δ_b^{Im} , $\hat{\Delta}_b^{\text{Im}}$: thin black solid curve; Δ_c^{Im} , $\hat{\Delta}_c^{\text{Im}}$: thin green dashed curve.

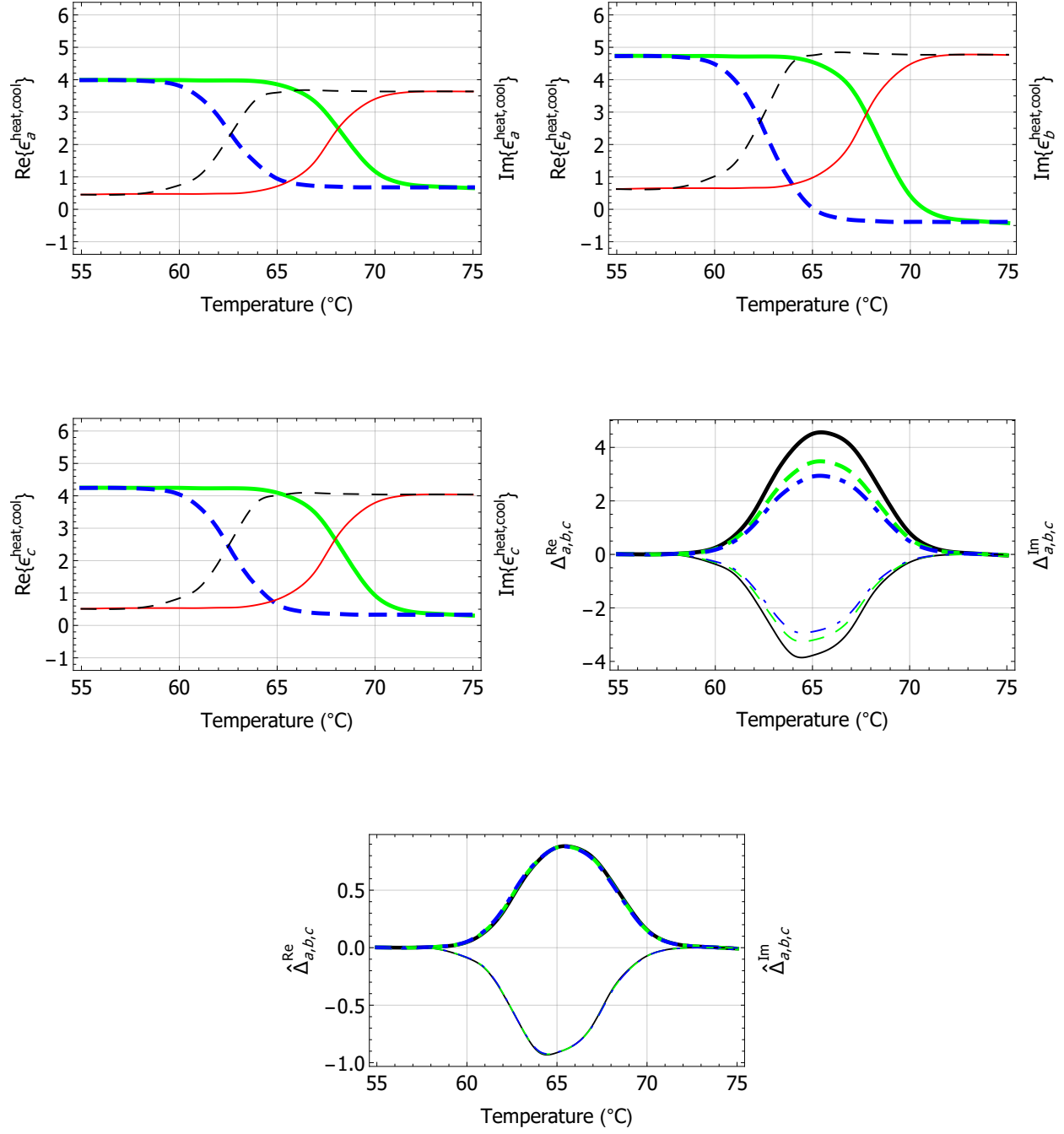


Figure 4: As Fig. 3 but for $\lambda_0 = 1550$ nm.

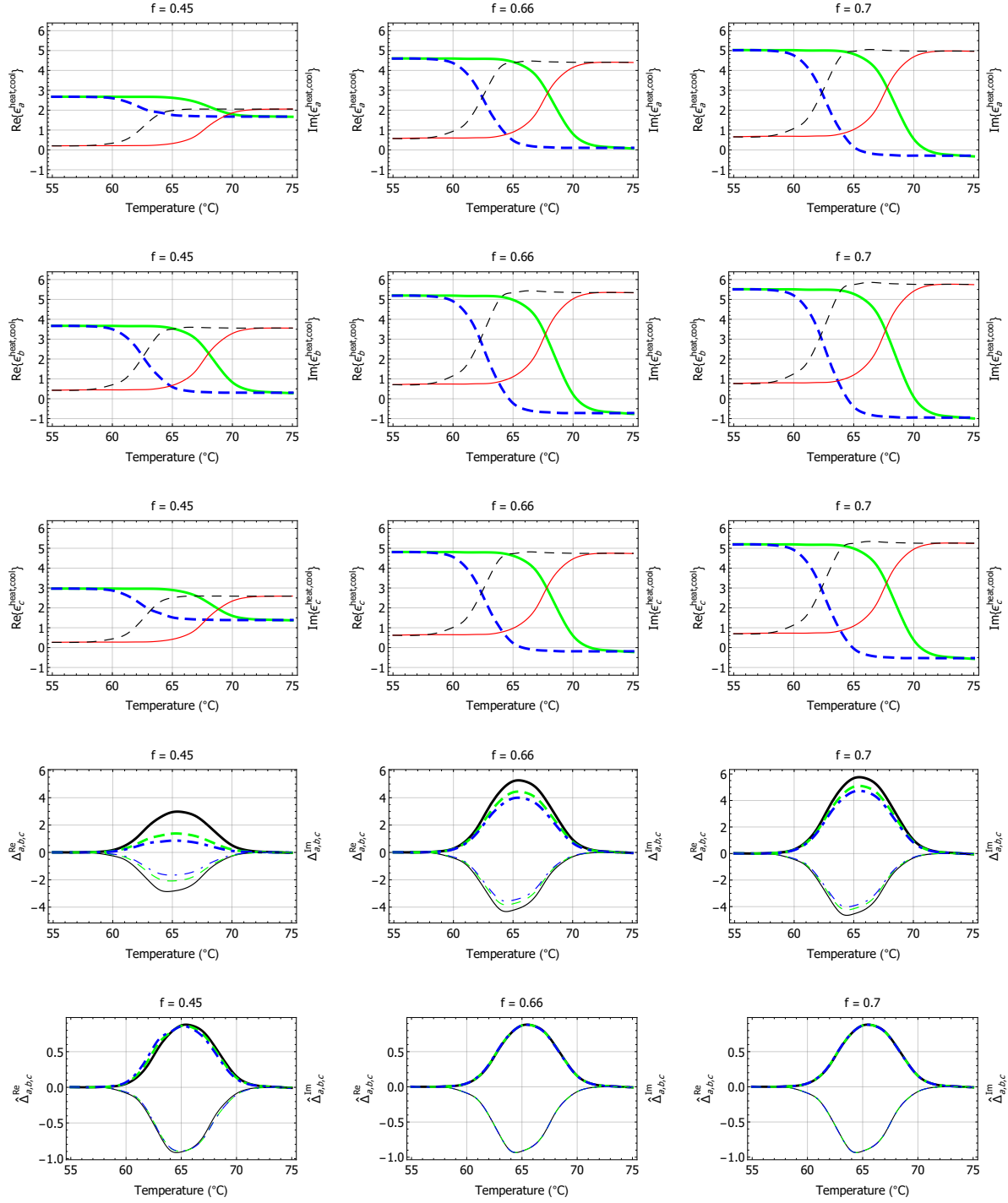


Figure 5: As Fig. 4 but for $f \in \{0.45, 0.66, 0.7\}$.

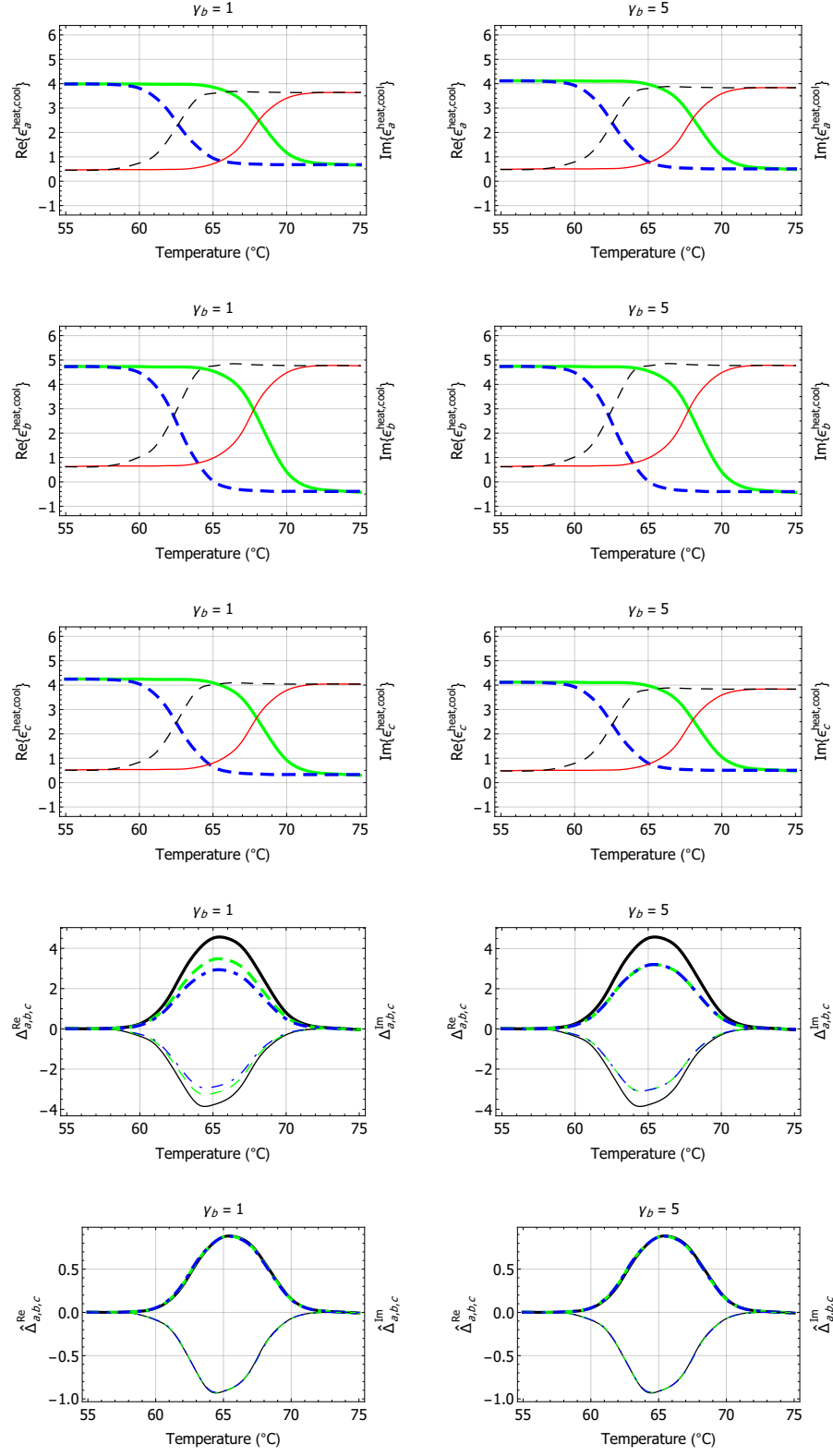


Figure 6: As Fig. 4 but for $\gamma_b \in \{1, 5\}$.